Supplementary

The effects of static local distortions vs. dynamic thermal motions on the stability and band gaps of cubic oxide and halide perovskites

Xin-Gang Zhao[1], Zhi Wang[1], Oleksandr I. Malyi[1] and Alex Zunger[1],*

Renewable and Sustainable Energy Institute, University of Colorado, Boulder, Colorado 80309

*Authors to whom correspondence should be addressed:
Alex.Zunger@colorado.edu, Alex.Zunger@gmail.com

A. Computational details of theoretical methods and technical setting:

Our *ab initio* calculations were performed within the framework of density-functional theory (DFT) using the plane-wave pseudopotential and total energy approach as implemented in the VASP code.[1] We used an open-source code named JAMIP[2] to manage and analyze the results. We used the PBEsol functional.[3] The electronic configurations for valence electrons in Cs, Ca, Sr, Ba, Ti, Pb, Sn, O, I are $5s^2 5p^6 6s^1$, $3s^2 3p^6 4s^2$, $4s^2 4p^6 5s^2$, $5s^2 5p^6 6s^2$, $3d^3 4s^1$, $6s^2 6p^2$, $5s^2 5p^2$, $2s^2 2p^4$, and $5s^2 5p^5$. We also tested the effect of using pseudopotentials with more valent electrons on i.e., 12 valences electron Ti ($3s^2 3p^6 4s^2 3d^2$) and Pb ($5s^2 5p^6 6s^2 6p^2$). Table S-I shows small differences in lattice constants (0.01 Å) and band gap (by 0.1 eV). In addition, the effect due to spin-orbit coupling (SOC) on the band gap shifts between a structure with distortion and a structure without distortion is also considered. The calculated error of band gap shifts is up to 0.03 eV, which is negligible (seen Table S-II). Therefore, in this work, we do not consider spin-orbit coupling for all the calculations.

The cell-internal atomic positions and lattice constants of cubic structures (1 fu/cell) were relaxed by keeping cubic symmetry with 8x8x8 k-grid. The calculated lattice constants listed in Table S-III show agreement to the experimental characterization within an absolute 1.1% error.

Polymorphous networks were modeled as supercells with 4×4×4 size. Relaxation was conducted by constraining the cell shape to cubic (otherwise, unconstrained relaxation will converge to the low-temperature low-symmetry ground states). We added initial random nudges on each atom in the 4×4×4 supercell with nudge amplitudes randomly selected between -0.15 to 0.15 Å with 0.01 Å steps. Then we relaxed the internal atomic positions by keeping fixed the lattice constants with Gamma-only point. The force threshold on each atom is set to 0.01 eV/Å.

The band gaps and total energy plotted in Fig. 2 are achieved by doing self-consistent calculations using PBEsol functional with 8x8x8 K-grids based on the 2×2×2 cubic supercell artificially applied single-mode distortions in fixed lattice constant.

a) *B site off-center:* we explored displacements with step length Δd=0.05 Å on B site atom along <100>, <110> and <111> directions within 1fu/cell structure. While the effects on internal

energy and band gap due to repulsion between atoms on A sites and atoms on B sites after atoms on B site having displacements are not considered.

b) *Compression or expansion:* Here, by using nominal cubic (Pm-3m, 1fu/cell) structure, we considered three types of possible distortions by applying compression and expansion along on c vector (<001> direction), a and b vectors (<100> and <010> directions, two directions simultaneously), and a, b, and c vectors (<100>, <010> and <001> three directions) with step length equal to 0.01 Å.

c) *Tilting modes:* Glazer's notions are well known to describe the local octahedral tilting/rotation in perovskites structure.[4] Nine special Glazer notions with unique rotation angles out of 23 possibilities are applied to the cubic structure by considering structural symmetry. For each individual tilting mode, we applied 0 to 18 ° of rotation angle on each octahedron along all the vectors simultaneously (if applicable) within 2×2×2 supercell.

d) *Breathing octahedral disproportionation mode and Jahn-Teller mode:* The breathing mode was considered by keeping lattice constant of 2×2×2 supercell. The modes are realized by artificially changing the bond length of B-X with frozen amplitudes of bond length change. For Jahn-Teller mode, there are two modes given the relatively different changes in the adjacent layer, named Q^{2+} and Q^{2-}.[5]

e) *Ab initio Molecular Dynamics simulation*: The DFT Molecular Dynamics (AIMD) simulations were performed in canonical ensemble with a Nosé-Hoover thermostat[6] for temperature control cubic $CaTiO_3$ at 2000 K using VASP, starting from the optimized T=0 geometry of the polymorphous network. We use supercells of 4×4×4 size, the PBEsol functional with Gamma-only k-grid. After 0.6 ps, the simulation is found to be equilibrated. We extracted the band gap values for the snapshot from 1.0 ps to ~2.0 ps. We analyzed the local distortions, including Ti off-center with respect to the center of octahedra, octahedral tilting with respect to cell vectors. These results are discussed in section IV.A.

f) *Unfolded band structure for supercells*: The importance of supercells in the present study is their allowance to account for symmetry-breaking modes excluded in small cells. At the same time, the disadvantage of supercells is that the ensuing dispersion relation is non intuitively complex because of extensive band folding. We, therefore, use our band unfolding

formalism to explore the electronic structure of a supercell (including DOWPs effects) unfolded into the primitive Brillouin zone of the simple Pm-3m structure.

The band folding formalism can be expressed as

$$|K_m\rangle = \sum_{i=1}^{N_k} \sum_n F(k_i, n; K, m)|k_i n\rangle \quad (1)$$

where $|K_m\rangle$ is the m-th electronic state at K in the supercell Brillouin zone, $|k_i n\rangle$ is the n-th electronic state at k_i in the primitive Brillouin zone. One can then unfold the supercell band structure by calculating the spectral weight $P_{Km}(k_i)$ from

$$P_{K_m}(k_i) = \sum_n |\langle K_m | k_i n\rangle|^2 (2)$$

which is the Bloch "preservation" of Bloch wavevector k_i in $|K_m\rangle$ when $E_n = E_m$. Finally, the effective band structure can be obtained using the spectral function $A(k_i, E)$,

$$A(k_i, E) = \sum_m P_{K_m}(k_i)\, \delta(E_m - E) \quad (3)$$

g) *Pair distribution function:*

The calculation for PDF from DFT optimized supercell structure of cubic $SrTiO_3$ is done using PDFgui software.[7] The, Q_{damp} and Q_{broad} are fixed at 0.042 and 0.016, while s_{ratio} and r_{cut} are set to 1.0 and 0, respectively, the same values used in Ref. [8] the scaling factor, δ_1, and atomic displacement parameters (ADPs) are fitted by PDFgui. For cubic $SrTiO_3$ supercell, the PDF of the short-range region (1.5–5.0 Å) is calculated using exactly the DFT total-energy minimized atomic positions, while the PDF of the long-range region (5.0–50.0 Å) is calculated using the same parameters as the short-range PDF (atomic positions, scaling factor, δ_1, and ADPs) but with a "padding" method, adding additional bulk-like nominal cubic $SrTiO_3$ all around the central cell, e.g., after the padding, the 512-f.u. supercell now contains 2560 atoms. This is to minimize the long-range periodicity error of the finite-size supercell. We use a weighted agreement factor R_w to assess the agreement between the calculated and observed PDF, which is given by

$$R_w = \sqrt{\frac{\sum_{i=1}^{n}[g_{obs}(r_i) - g_{calc}(r_i, P)]^2}{\sum_{i=1}^{n}[g_{obs}(r_i)]^2}}$$

Table S-I. Test of pseudopotential with a different number of electrons as valence electrons. The calculated lattice constant, band gap values of cubic $CaTiO_3$, $BaTiO_3$ and $CsPbI_3$ are tabulated. The differences of lattice constants $|\delta a|$ and band gap $|\delta E_g|$ values are also listed.

	Lattice constant, a (Å)			Band gap E_g (eV)		
	4 electrons	12 electrons	$\|\delta a\|$	4 electrons	12 electrons	$\|\delta E_g\|$
$CaTiO_3$	3.8757	3.8635	0.0115	2.03	2.06	0.03
$BaTiO_3$	3.9910	3.9860	0.0050	1.60	1.66	0.06
$CsPbI_3$	6.2428	6.2428	0.0000	1.18	1.19	0.01

Table S-II. Test of effect of spin-orbit coupling (SOC) on the calculated band gap shifts between cubic structure with octahedral rotation and cubic structure with non-local deformation for cubic $CaTiO_3$ ($a^-a^-a^-$ mode) and cubic $CsPbI_3$ ($a^0a^0b^-$ mode). The band gap values, and band gap shifts are tabulated.

	Without SOC			**With SOC**		
	$E_g(\boldsymbol{\theta}=0.0)$ (eV)	$E_g(\boldsymbol{\theta}=5.0)$ (eV)	ΔE_g (eV)	$E_g(\boldsymbol{\theta}=0.0)$ (eV)	$E_g(\boldsymbol{\theta}=5.0)$ (eV)	ΔE_g (eV)
$CaTiO_3$	1.70	1.96	0.26	1.69	1.97	0.28
$CsPbI_3$	1.18	1.23	0.05	0.10	0.18	0.08

Table S-III. Comparison of calculated lattice constant (a^{calc}) and experimental lattice constant (a^{exptl}) as well as the error of a^{calc} with respect to a^{exptl}.

Compounds	a^{exptl} (Å)	a^{calc} (Å)	error (%)
$CsPbI_3$	6.177[9]	6.243	+1.07
$CsSnI_3$	6.21 (500K)[10]	6.130	-1.29
$CaTiO_3$	3.82[11]	3.860	+1.05
$BaTiO_3$	4.017[12,13]	3.991	-0.65
$SrTiO_3$	3.90 (140K)[14]	3.908	+0.20

Besides the Glazer rotation, B site ferroelectric displacements and Jahn-Teller distortions (illustrated in Fig. 6 and Fig. 7), we also considered the single-mode, such as octahedral breathing, lattice expansion for cubic $ATiO_3$ (A=Ca, Sr, Ba) and halide perovskites $CsBI_3$ (B=Sn, Pb). These single modes cannot result in total energy lowering (see Fig. S-1 and S-2) in cubic oxide and halide

perovskites. According to the effects on the band gap within the considered range of distorted amplitudes, these single modes in cubic $ATiO_3$ can be roughly grouped into three types: (i) Jahn-Teller, off-center displacements result in gradually band gap blueshift as the amplitude of distortion increase, (ii) whereas the breathing mode lead to gradually band gap redshift as amplitude distortion increase, (iii) the lattice expansion and octahedral rotation mode can either result in band gap blueshift or redshift, which depends on the range of distorted amplitudes. Specifically, for cubic $ATiO_3$ (A=Ca, Sr, Ba), compression of lattice constants can result in band gap blueshift, lattice expansion can result in band gap redshift; octahedral tilting angle in range of 0-8° can result in band gap blueshift, while the redshift occurs when rotation angle over 8°. For halide perovskites $CsBI_3$ (B=Pb, Sn), these single modes can also be classified into three types: (i) octahedral rotation, B site off-center can result in band gap blueshift as amplitudes of distortion increase; (ii) Jahn-Teller distortion and breathing modes can lead to band gap redshift as amplitude increase; (iii) the compression of lattice constant lead to band gap decrease and lattice expansion result in band gap blueshift. The trends of energy lowering and band gap changes because of single-mode changes are not unique for perovskites, depending on the specific compositions of ABX_3 perovskites.

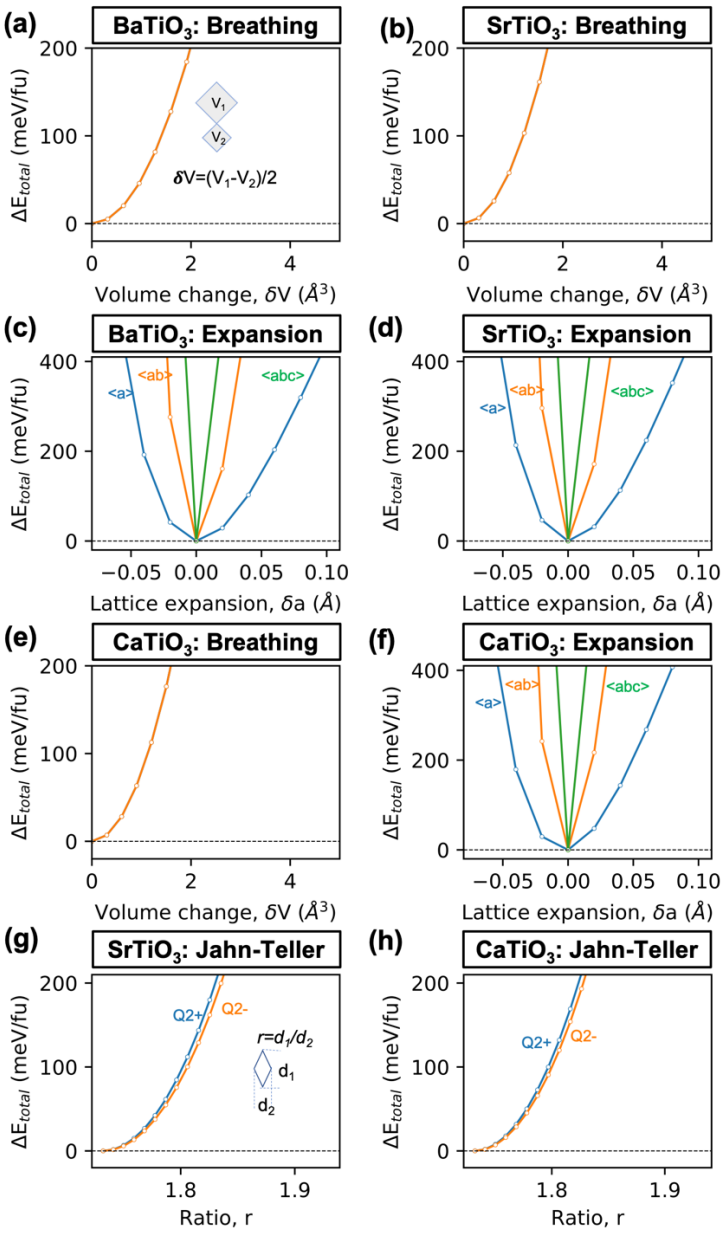

Figure S-1. Single-mode (one at the time) examination of potential energy lowering symmetry breaking in cubic oxide perovskites $BaTiO_3$ (a, c), $SrTiO_3$ (b, d, g) and $CaTiO_3$ (e, f, h) due to Distortions Off Wyckoff Positions (DOWPs) by DFT at T=0 using the PBEsol functional. Enthalpy changes as functions of the amplitude of (a, b, e) octahedral breathing mode; (c, d, f) lattice expansion; and (g, h) Jahn-Teller distortion (Q2+, Q2- modes). For lattice expansions on a, ab, abc directions, we use the minimal unit cells containing 1 fu/cell that already accommodate such a distortion, whereas evaluation of symmetry breaking Jahn-Teller distortions, breathing modes leading to disproportionation of octahedra, as well as the anti-ferroelectric displacement are all symmetry disallowed in the minimal unit cell structure, and are illustrated here for the 8 fu/cell. Such calculations involve a constrained energy minimization, where the shape and lattice vectors of the cell are kept as that of the global phase being investigated (here, cubic). All modes depicted of single modes are not energy lowering mode.

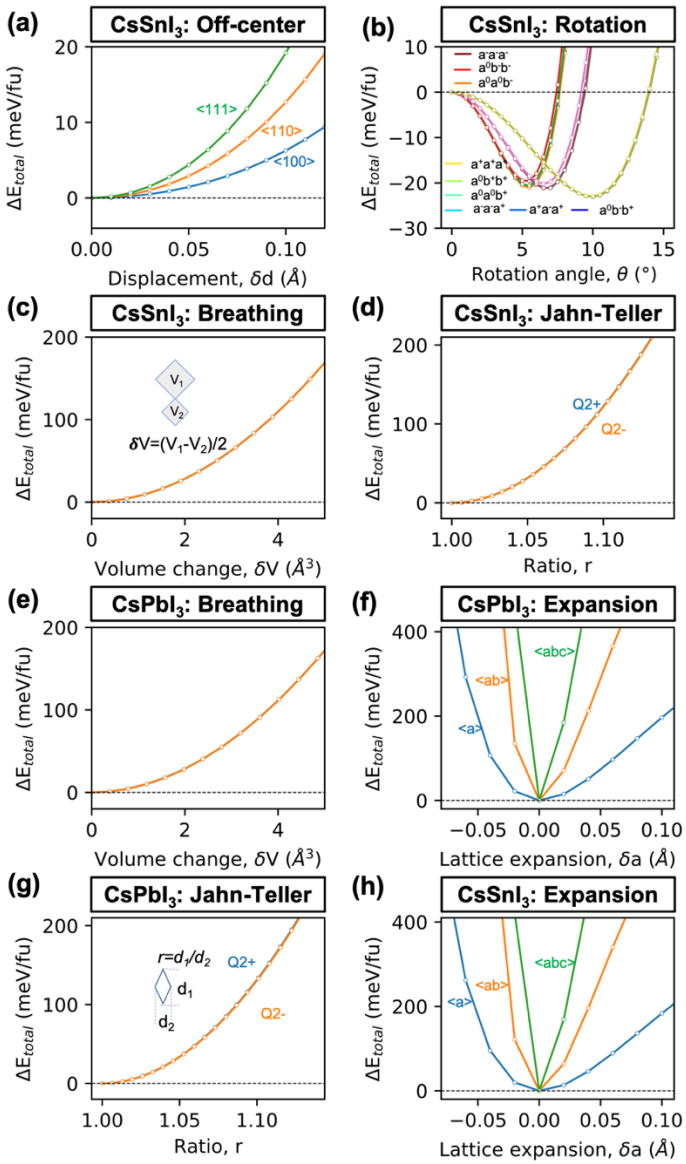

Figure S-2. Single-mode (one at the time) examination of possible energy lowering symmetry breaking in cubic halide perovskites $CsSnI_3$ (a, b, c, d, h) and $CsPbI_3$ (e, f, g) due to Distortions Off Wyckoff Positions (DOWPs) by DFT at T=0 using the PBEsol functional. Enthalpy changes as functions of the amplitude of (a) B site off-center displacements; (b) octahedral rotation; (c, e) octahedral breathing mode; (f, h) lattice expansion; and (d, g) Jahn-Teller distortion (Q2+, Q2- modes). All the single modes depicted here except tilting modes in $CsSnI_3$ cannot result in internal energy lowering.

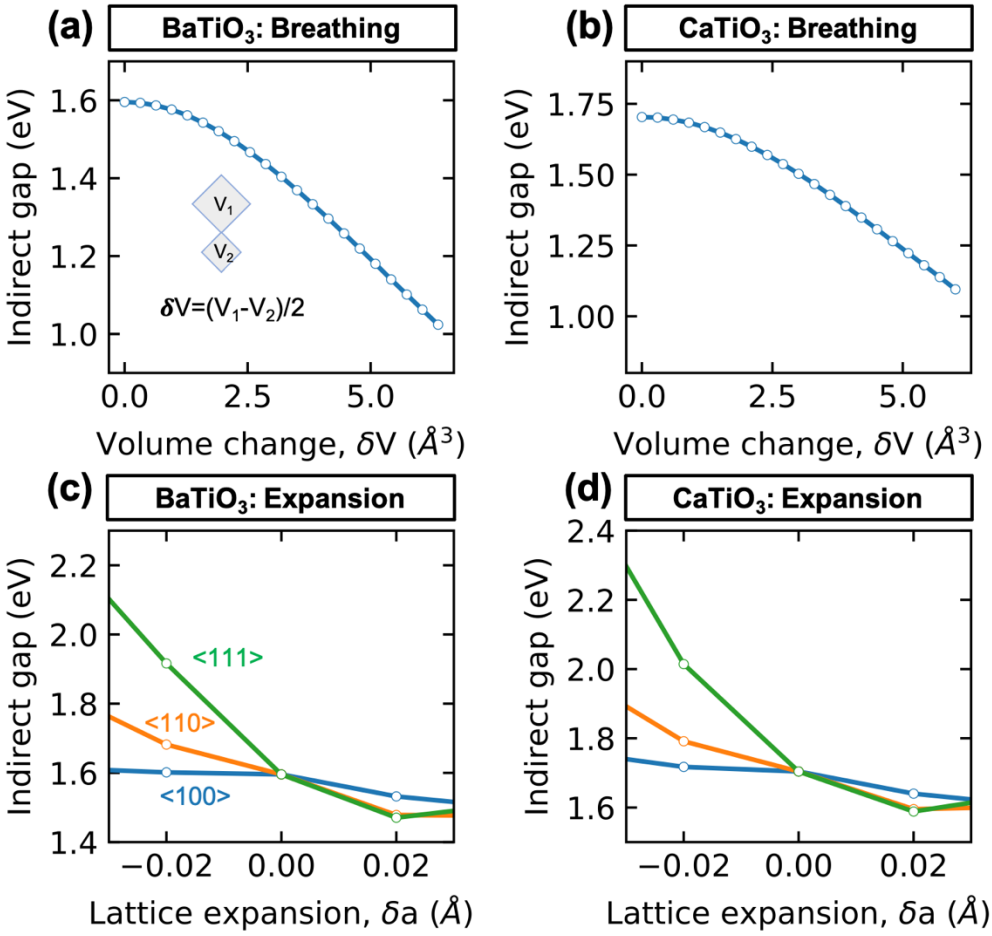

Figure S-3. Cubic oxide perovskites: Band gap changes as a function of different modes (a, b) breathing mode and (c, d) lattice expansion for cubic $BaTiO_3$ and cubic $CaTiO_3$.

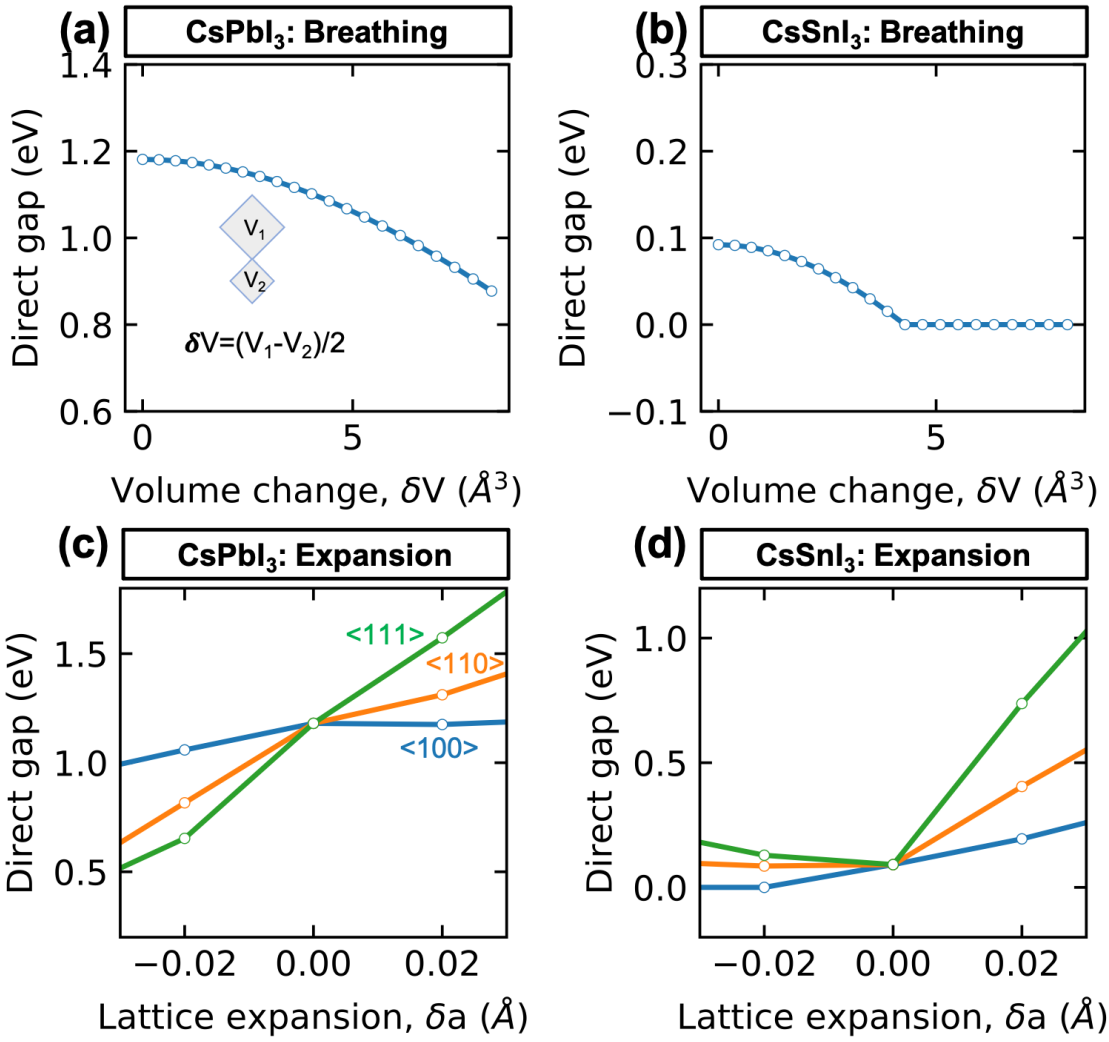

Figure S-4. Cubic halide perovskites: Band gap changes as a function of different modes (a, b) breathing mode and (c, d) lattice expansion for cubic $CsPbI_3$ and cubic $CsSnI_3$.

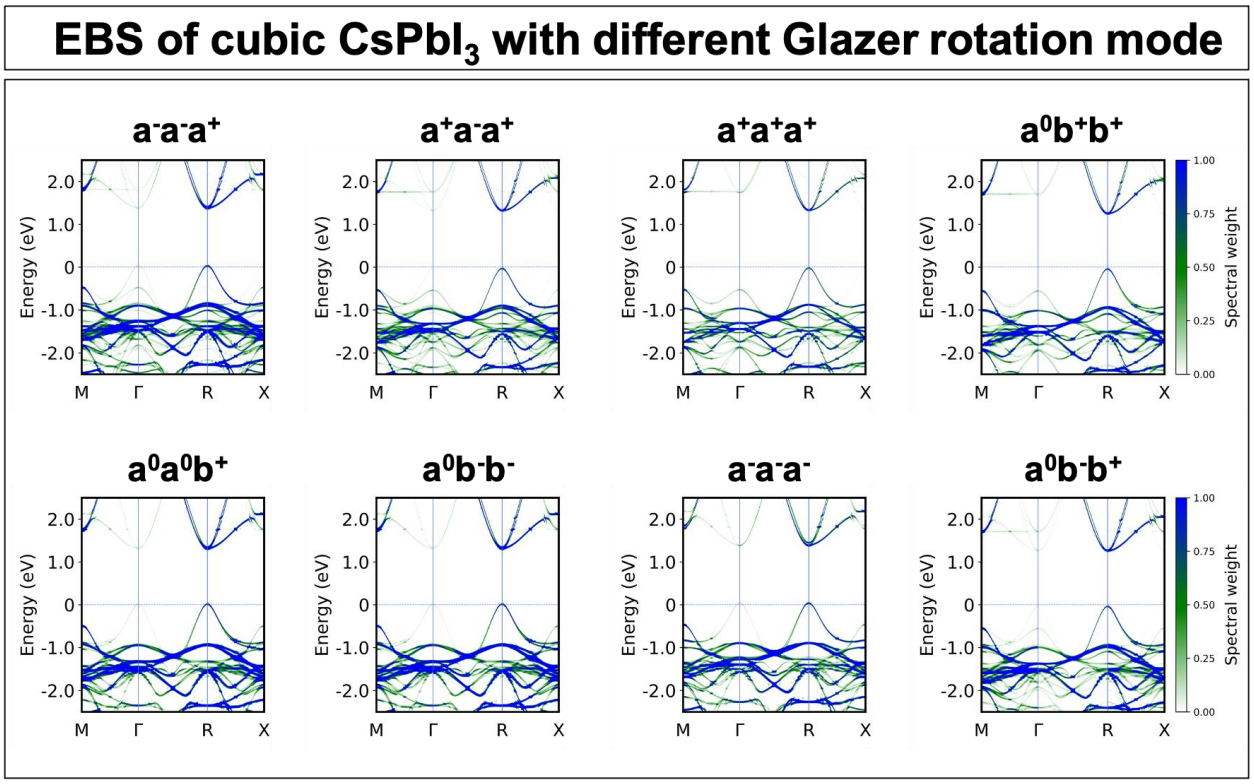

Figure S-5. The effect band structure (EBS) of $CsPbI_3$ in 2×2×2 supercell with single Glazer notation. For cubic $CsPbI_3$, the EBS always shows a direct gap at the R point. Different octahedral rotation modes result in similar band edges states, which is significantly different from $CaTiO_3$ (Fig. 9 main text)

References:

[1] G. Kresse, J. Furthmüller, Phys. Rev. B 54 (1996) 11169–11186.

[2] X.-G. Zhao, K. zhou, B. Xing, R. Zhao, S. Luo, T. Li, Y. Sun, G. Na, J. Xie, X. yang, X. Wang, X. Wang, X. He, J. Lv, Y. Fu, L. Zhang, ArXiv:2103.07957 (2021).

[3] J.P. Perdew, A. Ruzsinszky, G.I. Csonka, O.A. Vydrov, G.E. Scuseria, L.A. Constantin, X. Zhou, K. Burke, Phys. Rev. Lett. 100 (2008) 136406.

[4] A.M. Glazer, Acta Cryst B, Acta Cryst Sect B, Acta Crystallogr B, Acta Crystallogr Sect B, Acta Crystallogr B Struct Crystallogr Cryst Chem, Acta Crystallogr Sect B Struct Crystallogr Cryst Chem 28 (1972) 3384–3392.

[5] J. Varignon, M. Bibes, A. Zunger, Nature Communications 10 (2019) 1658.

[6] D. Frenkel, B. Smit, Understanding Molecular Simulation: From Algorithms to Applications, Elsevier, 2001.

[7] C.L. Farrow, P. Juhas, J.W. Liu, D. Bryndin, E.S. Božin, J. Bloch, T. Proffen, S.J.L. Billinge, J. Phys.: Condens. Matter 19 (2007) 335219.

[8] A.N. Beecher, O.E. Semonin, J.M. Skelton, J.M. Frost, M.W. Terban, H. Zhai, A. Alatas, J.S. Owen, A. Walsh, S.J.L. Billinge, ACS Energy Lett. 1 (2016) 880–887.

[9] G.E. Eperon, G.M. Paternò, R.J. Sutton, A. Zampetti, A.A. Haghighirad, F. Cacialli, H.J. Snaith, J. Mater. Chem. A 3 (2015) 19688–19695.

[10] I. Chung, J.-H. Song, J. Im, J. Androulakis, C.D. Malliakas, H. Li, A.J. Freeman, J.T. Kenney, M.G. Kanatzidis, J. Am. Chem. Soc. 134 (2012) 8579–8587.

[11] V.V. Lemanov, A.V. Sotnikov, E.P. Smirnova, M. Weihnacht, R. Kunze, Solid State Communications 110 (1999) 611–614.

[12] M. Yashima, M. Tanaka, J Appl Cryst 37 (2004) 786–790.

[13] K. Suzuki, K. Kijima, Journal of Alloys and Compounds 419 (2006) 234–242.

[14] F.W. Lytle, Journal of Applied Physics 35 (1964) 2212–2215.